Ternary NiAuPt Nanoparticles on Reduced Graphene Oxide as Catalysts toward the Electrochemical Oxidation Reaction of Ethanol

Abhijit Dutta[†] and Jianyong Ouyang*

Department of Materials Science and Engineering, National University of Singapore, 7 Engineering Drive 1, 117576 Singapore

S *Supporting Information*

ABSTRACT: This article presents a facile one-pot synthetic method to prepare ternary NiAuPt nanoparticles on reduced graphene oxide (rGO) nanosheets (NiAuPt-NGs) through the simultaneous chemical reduction of metal precursors and GO in solution and an investigation of NiAuPt-NGs as electrocatalysts toward ethanol oxidation reaction (EOR). The NiAuPt nanoparticles grow on the rGO sheets after the chemical reduction of their precursors. They consist of tightly coupled nanostructures of Ni, Au, and Pt, which have neither an alloy nor a core−shell structure, as revealed by X-ray diffraction, transmission electron microscopy, and X-ray photoelectron spectroscopy. As indicated by the Raman spectra, GO is reduced to rGO more completely in the presence of the metal precursors than in the absence of the metal precursors. The electrocatalysis of NiAuPt-NGs toward EOR in alkaline medium was investigated by cyclic voltammetry, chronoamperometry, and impedance spectroscopy. NiAuPt-NGs can effectively catalyze EOR. The ternary NiAuPt-NGs give rise to a high peak current density for EOR, which is more than 8 times higher than that on the monometallic Pt-NGs, 4 times higher than that on the bimetallic NiPt-NGs, and almost 2 times higher than that on the bimetallic AuPt-NGs. In addition, NiAuPt-NGs substantially lower the onset potential for EOR. It is −803 mV vs SHE, which suggests the excellent tolerance of NiAuPt-NGs against the residues of EOR. The high electrocatalytic activity of NiAuPt-NGs is attributed to the synergetic effect of the three nanostructured metals for EOR.

KEYWORDS: *electrocatalysis, ethanol oxidation reaction, ternary nanoparticles, NiAuPt, durability*
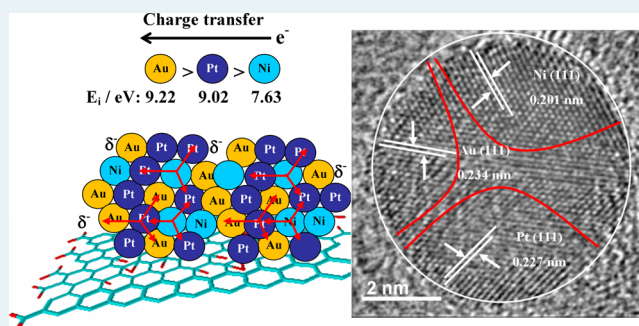
1. INTRODUCTION

Direct ethanol fuel cells (DEFCs) have attracted considerable attention over the past several decades because of their high energy conversion efficiency, which can be up to 8.01 kWh kg^{-1}, low operating temperature, and eco-friendly energy conversion process.[1−3] DEFCs are attractive as the power sources particularly for mobile, stationary, and portable applications, because it is convenient to produce, transport, and store the liquid ethanol fuels.[1−5] Nevertheless, a major challenge in commercializing DEFCs lies in the need for highly active catalysts for the ethanol oxidation reaction (EOR) in acid or alkaline media, because EOR has sluggish kinetics. The complete oxidation of an ethanol molecule into CO_2 involves 12 electrons and the cleavage of the C−C bond.[1−6] In addition, the permeation of ethanol through the Nafion membrane can lead to a depolarizing reaction at the cathode.[6] The sluggish EOR is related to the absorbance of intermediates such as CO produced during EOR on the catalyst surface. The CO absorbance problem can be relieved by using alkaline media, since the intermediates bond to the electrocatalyst in alkaline media more weakly than in acidic media.[7]

The current popular electrocatalyst for EOR is Pt/C.[8,9] However, pure Pt is readily poisoned by the reaction intermediates, even in alkaline media.[10−12] It has been revealed

that the catalytic activity is affected by the structure and composition, such as the interatomic distance, band vacancy, number of neighboring metal atoms, and the metal content on the surface.[13,14] The catalytic activity of a metal catalyst can be enhanced if other metals are present in the catalyst, because the electron transfers among the metals can improve the surface function toward the electrochemical reactions. Moreover, some metal atoms can be presented as oxides on the surface of multiple metals. The oxides can prevent the CO adsorption on the catalyst surface by supplying oxygen-containing species such as OH. Thus, attempts have been made to improve the catalytic activity of Pt through the incorporation of a second metal, such as Ru, Rh, Au, Sn, Pd, Ni, and so on.[13−17] It has been reported that Pt-based alloy or bimetallic nanoparticles, such as PtRu, PtNi, PtPd, PtAu, and PtRh, can exhibit high electrocatlytic activity toward the methanol oxidation reaction and EOR.[18,19] Among the Pt-based binary metal nanoparticles, PtRu alloy nanoparticles can exhibit the highest electrocatalytic activity toward EOR. This is attributed to the oxophilic nature of Ru and the formation of oxygenated species, which can

inhibit the adsorption of CO on Pt.[18−20] However, Ru dissolves in the electrolyte during the operation, and the dissolved Ru ions contaminate the membrane and degrade the catalytic activity.[1,21−24] It has been also reported that Ni can improve the catalytic activity of Pt.[24−31] The advantage for Ni is that it does not dissolve into the electrolyte at the potential range for EOR because its surface is passivated by $Ni(OH)_2$.[6,32−35] NiPt and PtRuNi nanoparticles without any supporting material have been investigated as the electrocatalysts for the methanol oxidation reaction.[33,36] For instance, Mu et al. observed higher catalytic activity of NiPt toward the CO oxidation reaction in comparison to that of Pt.[31] They attributed the improvement to the synergetic effects of Pt and Ni. Apart from Ni, Au has also been incorporated with Pt, since Au nanoparticles can have an amazing electrocatalytic activity toward the oxidation reactions of CO, methanol, and ethanol.[37−47] In addition, Au can modify the electronic structure of Pt.[43] The incorporation of Au can reduce the poisoning problem of Pt by removing intermediate species such as CO and/or providing oxygenated species. Recently, Au was also incorporated into PtRu to improve the catalytic activity.[40,41] Hence, it is interesting to incorporate both Ni and Au into Pt. To the best of our knowledge, there has been no report on the preparation of NiAuPt nanoparticles on reduced graphene oxide (rGO) sheets and their application as electrocatalysts toward EOR in alkaline media. In fact, ternary metallic nanoparticles have been much less explored than binary metallic nanoparticles for electrocatalytic applications because of the complexity of the ternary systems.

In this work, ternary NiAuPt nanoparticles were prepared on rGO sheets (NiAuPt-NGs) by a one-pot synthetic method, and the NiAuPt-NGs were investigated as the electrocatalysts for EOR in alkaline media. rGO sheets have been selected as the supporting material for NiAuPt nanoparticles because they have high surface area and high electrical conductivity.[45−55] They can thus be more effective supporting materials for the metal nanoparticles than the conventional carbon black. When GO is used as a precursor for the preparation of metal naoparticles on rGO, the functional groups on GO can serve as the anchoring sites for the metal nanoparticles.[56−58] We observed the synergetic effects of the three components of NiAuPt on EOR. Pt facilitates ethanol dehydrogenation, and Ni and Au concurrently contribute to the removal of the adsorbed reaction intermediates. NiAuPt-NGs exhibit much higher electrocatalytic activity toward EOR than both the monometallic Pt-NGs and bimetallic AuPt-NGs and NiPt-NGs.

2. EXPERIMENTAL SECTION

2.1. Materials. Highly pure natural graphite (SP-1 graphite, purity >99.99%) powder was purchased from Bay Carbon Inc. It had an average particle size of ∼30 μm. Other chemicals with a purity of analytical grade, including $H_2PtCl_6·6H_2O$, $HAuCl_4·3H_2O$, 5 wt % Nafion ionomer solution, 2-propanol, $KMnO_4$, $NaBH_4$, $NaNO_3$, H_2O_2, H_2SO_4, NaOH, ethanol, hydrazine hydrate, and HCl, were supplied by Sigma-Aldrich. All chemicals were used as received without further purification.

GO was synthesized according to a modified Hummer method.[59,60] Briefly, 0.5 g of graphite, 0.5 g of $NaNO_3$ and 23 mL of concentrated H_2SO_4 were placed in a 250 mL round-bottom flask in an ice bath. The mixture was vigorously stirred. A 3 g portion $KMnO_4$ was slowly added to the mixture. The ice bath was removed after 30 min, and the dark green solution was stirred at 40 °C for another 1 h. Then, 70 mL of water was added very slowly, and the reaction vessel was bathed in boiling

water for 30 min. A 10 mL portion of 30% H_2O_2 and 150 mL of deionized (DI) water were subsequently added. The precipitate was centrifuged and washed repeatedly with 5% HCl, ethanol, and DI water to remove the metal ions and acid. Finally, the slurry was redispersed in DI water and subsequently exfoliated to GO nanosheets by ultrasonication.

The metal nanoparticles on rGO were prepared by the simultaneous reduction of GO and metal precursors with $NaBH_4$. The concentration of each precursor, $NiCl_2$, H_2PtCl_6, and $HAuCl_4$, was 0.002 M, and the GO concentration was 0.5 mg mL^{-1} in water. The mixture was ultrasonicated for 30 min, followed by stirring for 1 h. The pH value of the solution was adjusted to 8−9 by adding 1 M KOH aqueous solution. The solution was refluxed in a water bath at 75 °C, and 30 mL of 0.05 M $NaBH_4$ was added dropwise. The yellowish brown solution turned black. The black NiAuPt-NGs were rinsed with copious DI water and finally dried at 100 °C in a vacuum oven for 3−4 h. Control nanomaterials, including NGs, Pt-NGs, AuPt-NGs, and NiPt-NGs, were also synthesized through a similar procedure. The molar ratio of the metal precursors for binary metal nanoparticles was also kept at 1:1.

2.2. Materials Characterization. The crystallinity of the catalysts was studied using a SEIFERT 2000 X-ray diffractometer equipped with a Cu Kα radiation source (λ = 0.1540 nm). The X-ray diffraction (XRD) patterns were identified by referring to the JCPDS files. The Scherrer and Bragg formulas were used to calculate the mean diameter and the lattice parameters for each sample. An inductively coupled plasma atomic emission spectrometer (ICP-AES, Jarrell-Ash, and ICAP 9000) was used to detecte the composition of the catalysts. Thermogravimetric analysis (TGA) was performed with a PerkinElmer TGA-7 instrument. The heating rate was 10 °C min^{-1}. Raman spectra were recorded with a Nicolet NXR FT-Raman spectrometer using an Ar ion laser with an excitation wavelength of 514.5 nm. Scanning electron microscopic (SEM) images were taken with a Zeiss Supra 40 FE SEM instrument. Tunneling electron microscopic (TEM) images were acquired with a HRTEM instrument (JEOL Model 2010F) operated at an accelerating voltage of 200 kV. The TEM samples were prepared by suspending the materials on standard carbon-coated Cu grids. Energy-dispersive X-ray spectra (EDX) were obtained using the transmission electron microscope equipment with a Link ISIS EDX detector. The X-ray photoelectron spectra (XPS) were taken using an Axis Ultra DLD X-ray photoelectron spectrometer equipped with a 150 W Al Kα radiation source. The resolutions were 1 eV for XPS survey scans and 0.05 eV for the XPS fine scans. The CasaXPS software version 2.3.14 program was used to subtract the Shirley background, analyze the composition, and deconvolute the XPS peaks. The survey and fine-scan XPS spectra were calibrated with the C 1s band at 284.5 eV.

2.3. Electrode Preparation and Electrochemical Studies. A catalyst ink was prepared by mixing the catalyst with a 5 wt % Nafion ionomer solution in a cosolvent of 70% 2-propanol and 30% water. The catalyst ink was deposited on graphite block/plate saw cut finish grade with a thickness of approximately 2 mm.[6] The catalyst loading was kept at 0.50 mg cm^{-2}, and the geometrical surface area of the graphite block was 0.65 cm^2. Electrochemical measurements were conducted in a three-electrode cell using a Autolab 302N potentiostat/galvanostat. Ag/AgCl, Pt foil, and a catalyst/graphite were used as the reference, counter, and working electrodes, respectively. The impedance data were analyzed with NOVA

Version 1.10 software. All electrochemical experiments were performed in a solution of 0.5 M NaOH and 1 M ethanol. The electrolyte was purged with highly pure N_2 for 30 min before each measurement.

3. RESULTS AND DISCUSSION

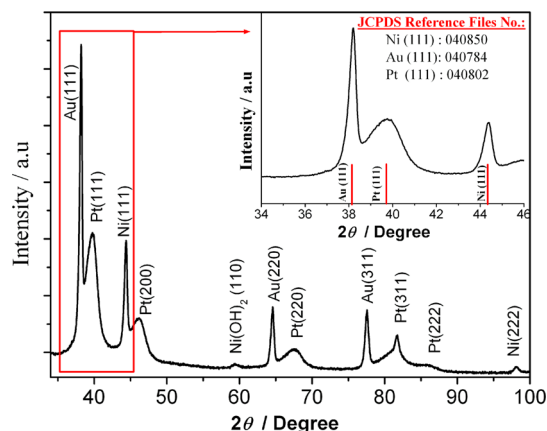**3.1. Structure of NiAuPt-NGs.** The metal loading on rGO was analyzed by TGA (Figure S1 in the Supporting

Figure 1. XRD pattern of $Ni_{40}Au_{33}Pt_{27}$-NGs catalyst. The inset is the magnified view of the (111) peak.

Information). The mass percentages of metals with respect to rGO are 19.8%, 20.3%, 20.1%, and 19.3% for NiAuPt-NGs, AuPt-NGs, NiPt-NGs, and Pt/C, respectively.

The crystal structures of the ternary, binary, and unary metal nanoparticles on rGO were analyzed by XRD. The XRD patterns for the binary and unary metal nanoparticles on rGO are presented in Figure S2 in the Supporting Information. The XRD results indicate that all of them have a face-centered cubic (fcc) structure. The XRD patterns of (111), (200), and (220) were observed for AuPt-NGs, NiPt-NGs, Pt-NGs, and Au-NGs.[6,61] For the unary nanoparticles on NGs, the XRD patterns of (111), (200), and (220) appear at 39.8, 46.3, and 67.5° for Pt-NGs, at 38.2, 44.4, and 64.6° for Au-NGs, and at 44.5, 51.8, and 76.3° for Ni-NGs. For the binary nanoparticles on NGs, the diffraction peaks of Pt(111), Pt(200) and Pt(220) are at 39.2, 46.1, and 67.2° and at 40.1, 46.6, and 67.9° for AuPt-NGs and NiPt-NGs, respectively. All three XRD patterns of Pt(111), Pt(200), and Pt(220) slightly shift to lower degrees for AuPt-NGs than for Pt-NGs. In contrast, the three XRD patterns slightly shift to higher degrees for NiPt-NGs than for Pt-NGs. This suggests that the binary nanoparticles AuPt-NGs and NiPt-NGs, have an alloy structure.[6,56]

The ternary NiAuPt nanoparticles on NGs exhibit a structure different from that of the binary metal nanoparticles. Diffraction patterns corresponding to Au, Pt, and Ni were observed[62] (Figure 1). According to their respective JCPDS files, the three patterns at 38.3, 39.6, and 44.5° are the (111) facet of Au, Pt, and Ni, repectively (inset of Figure 1). The pattern at 44.7° corresponds to the Au(200) plane, and the two patterns at 64.8 and 67.7° are assigned to Au(220) and Pt(220), respectively. No obvious shift in the diffraction patterns was observed in comparison with the unary metal nanoparticles. These results suggest that Ni, Au, and Pt do not form alloy. The diffraction patterns at 39.3, 44.7, and 64.8° are assigned to Au(111), Au(200) and Au(220), indicating a Au-rich phase.[62,63]
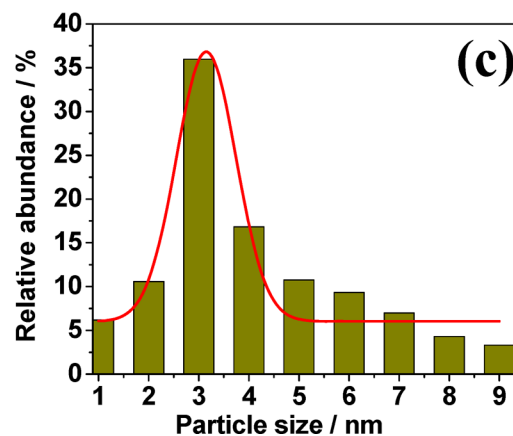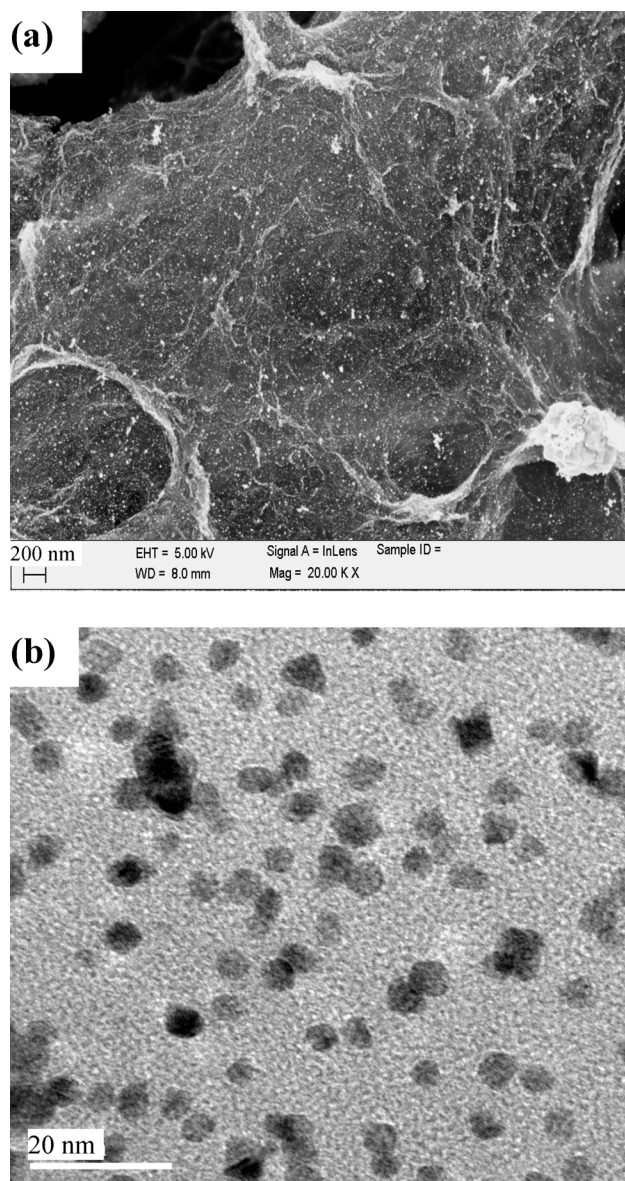

Figure 2. (a) SEM and (b) TEM images of NiAuPt-NGs. (c) Particle size histogram of NiAuPt nanoparticles on NGs.

Similarly, the XRD patterns at 39.6 and 67.7° are due to Pt(111) and Pt(220), respectively. The XRD pattern at 44.5° originates from Ni(111). These results suggest the existence of
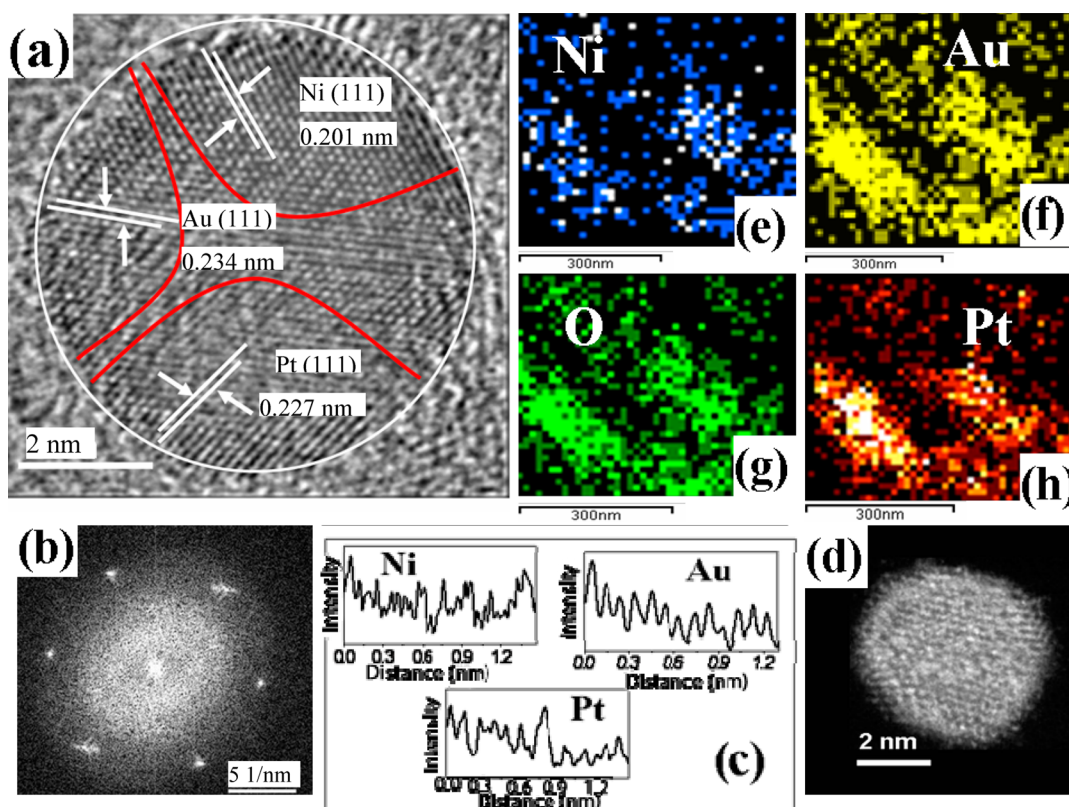
Figure 3. (a) HRTEM image of the fringe pattern with three different spacings. (b) Selected area diffraction patterns. (c) Line profile analysis of fringe fingerprints for *d*-spacing evaluation of NiAuPt-NGs. (d) HAADF-STEM image. (e)−(h) EDX mappings of NiAuPt-NGs.

Pt-rich and Ni-rich phases in the nanoclusters as well.[64] The binary metals form alloy nanoparticles, whereas the ternary metals cannot form alloy. This can be attributed to the different compositions of the metals in the binary and ternary materials, because the phase of metal mixtures is sensitive to their composition. The observation of the $Ni(OH)_2(110)$ plane in both ternary NiAuPt-NGs and binary NiPt-NGs is worth noting. However, there is no XRD pattern for any oxide of Pt or Au.[63] The crystallinity of the nanoparticles can be obtained in terms of the full width at half-maximum (fwhm) of the diffraction bands in terms of the Debye−Scherrer equation.[6,61,62] The FWHMs of the (111) diffraction planes of the nanoparticles were determined by using the Maud software, and they were used to calculate the average particle size. The metal crystallite sizes are 3.3 and 3.7 nm for AuPt-NGs and NiPt-NGs, respectively. Three crystallite sizes were calculated for NiAuPt-NGs owing to the observation of three (111) plane patterns. The sizes are 3.1, 3.5, and 4.1 nm for the Au-rich, Pt-rich, and Ni-rich phases, respectively (Table S1 in the Supporting Information).[6,65]

The microstructure of the metal nanoparticles on rGO sheets was investigated by SEM and TEM. The SEM image of NiAuPt-NGs indicates that the nanoparticles are well dispersed on the rGO sheets (Figure 2a). The TEM image shows that the nanoparticles grow uniformly on the rGO surface (Figure 2b). The particle size distributions, on the basis of statistics over 100 nanoparticles as shown in the TEM images, indicate a narrow size distribution (Figure 2c). The average size of NiAuPt nanoparticles is about 3.4 nm, which agrees with the XRD analysis (see Table S1 in the Supporting Information for a detailed analysis). The TEM images and particle size histogram of the other catalysts have also been compared in Figure S3 in

the Supporting Information. The point-resolved EDX spectrum has been collected from a number of individual particles. It reveals that the nanoparticles grow with an ensemble of atoms of the individual metals, including Ni, Au, and Pt (Figure S4 in the Supporting Information). In addition, no chloride was observed by EDX. Thus, there is no metal precursor in the product. In terms of the ICP-AES of NiAuPt-NGs (Table S1), the Ni:Au:Pt atomic ratio is 40:33:27.

$Ni_{40}Au_{33}Pt_{27}$-NGs was further characterized by high-resolution TEM (HRTEM) (Figure 3a). The HRTEM image indicates the crystalline structure for a single nanoparticle. The electron diffraction patterns and the FFT patterns are utilized to determine the interplanar spacing (Figure 3b,c). The lattice spacings are 0.201, 0.234, and 0.227 nm, which correspond to the (111) planes of Ni, Au, and Pt, respectively. Hence, $Ni_{40}Au_{33}Pt_{27}$-NGs consists of three tightly coupled Ni-rich, Au-rich, and Pt-rich zones. Both the TEM and XRD results imply that Ni, Au, and Pt do not form an alloy. This is also supported by high-angle annular dark-field scanning TEM (HAADF-STEM) images of $Ni_{40}Au_{33}Pt_{27}$-NGs (Figure 3d) and the related mappings of Ni, Au, Pt, and O (Figure 3e−h).

XPS was employed to further substantiate the surface composition and the surface oxidation states of $Ni_{40}Au_{33}Pt_{27}$-NGs. The XPS bands at 71.4 and 74.7 eV are due to metallic Pt, and the bands at 84.0 and 87.7 eV originate from metallic Au (Figure 4a).[39,66−68] The Ni 2p XPS bands indicate the presence of both metallic Ni and Ni^{2+} species (Figure 4b). The Ni^{2+} species are presumably nickel oxides and/or nickel hydroxides.[69] Interestingly, the Ni 2p signal shows a complex structure with strong satellite signals with binding energy higher than that of the main XPS bands, characteristic of multielectron excitation.[66,70] After the consideration of these shakeup peaks,
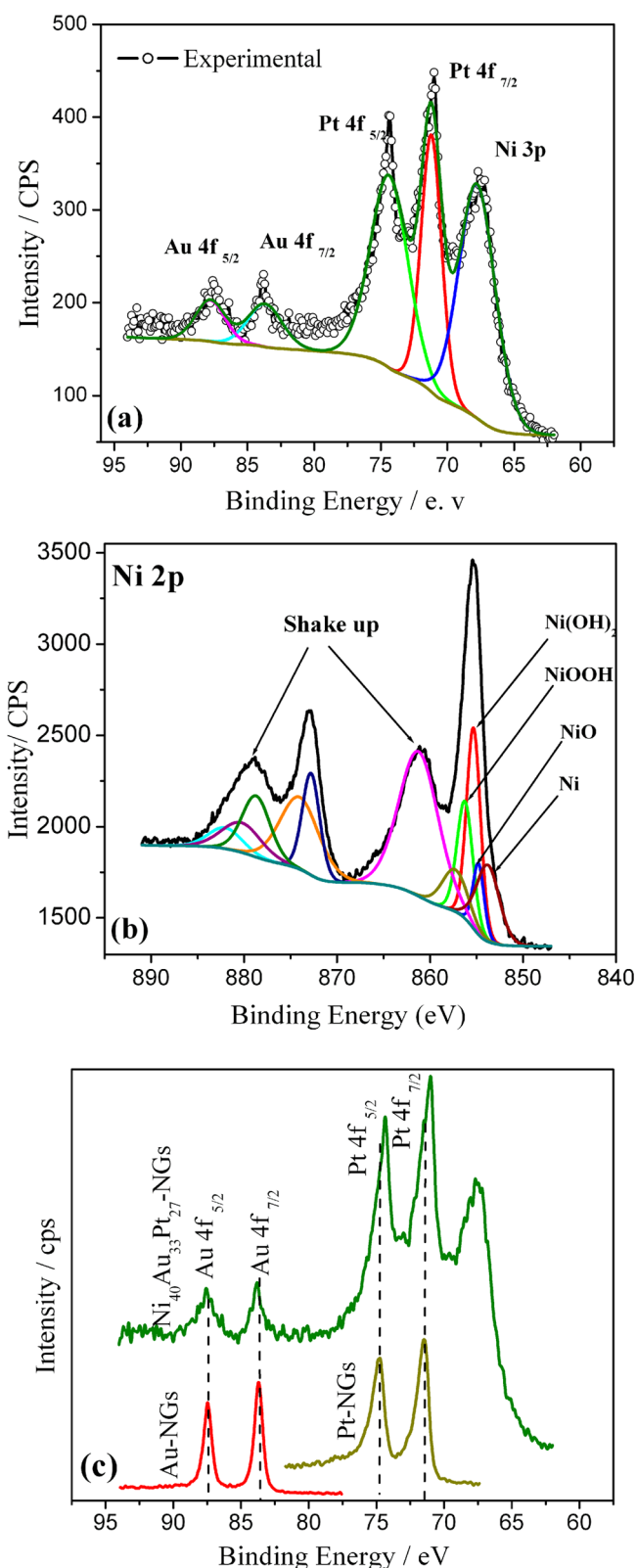
Scheme 1. Schematic Representation of the Charge Distribution in rGO-Supported Ni$_{40}$Au$_{33}$Pt$_{27}$-NGs Catalysts

NiOOH. The area percentages of the four bands are 5.61%, 21.33%, 38.55%, and 34.51%, respectively.

The binding energies of Ni$_{40}$Au$_{33}$Pt$_{27}$ are different from those of individual metals. As shown in Figure 4c, the Pt 4f binding energies of NiAuPt-NGs are higer than those of Pt-NGs. On the other hand, the Au 4f binding energies of NiAuPt-NGs are lower than those of Au-NGs. This can be attributed to the electron transfer among the three types of metal atoms. The ionization energies of Ni, Pt, and Au are 7.63, 9.02, and 9.22 eV, respectively. The possible charge transfers among the metals are illustrated in Scheme 1. The electron transfer induced change in the electronic structure of the metals can improve the electrocatalytic activity.

GO, rGO, and Ni$_{40}$Au$_{33}$Pt$_{27}$-NGs were also characterized by Raman spectroscopy (Figure 5a). The two peaks at 1355 and 1593 cm^{-1} are the D and G bands, respectively. Usually, the D band is correlated with the breathing mode of k-point phonons of A$_{1g}$ symmetry, while the G band is related to the E$_{2g}$ phonons of sp^2 carbon atoms.[71] The intensity ratio of the D to G band, I_D/I_G, can be used to evaluate the reduction degree of GO. The I_D/I_G ratio increases after the reduction of GO.[71,72] Ni$_{40}$Au$_{33}$Pt$_{27}$-NGs show a higher I_D/I_G value (1.33) than GO (0.91), signifying a successful reduction of GO. Moreover, the I_D/I_G ratio of NiAuPt-NGs is even higher than that (1.03) of rGO without metal nanoparticles. This implies that the metal nanoparticles or metal precursors can facilitate the GO reduction.[67] The more complete reduction of GO can lead to higher conductivity for rGO. This can facilitate the charge transport through the catalyst. Moreover, the different I_D/I_G ratio of Ni$_{40}$Au$_{33}$Pt$_{27}$-NGs in comparison to that of rGO also suggests an electronic interaction between rGO and the metal nanoparticles. A similar observation was reported by Naumenko et al.[73]

GO, rGO, and Ni$_{40}$Au$_{33}$Pt$_{27}$-NGs were studied by XPS as well. The C 1s XPS spectrum of GO can be deconvoluted into four components at 284.8, 286.8, 287.8, and 289.0 eV (Figure 5b). They correspond to C–C and C=C, C–O, C=O, and O–C=O groups, respectively. The C–C band is predominant for rGO (Figure 5c). Interestingly, the C–O intensity of Ni$_{40}$Au$_{33}$Pt$_{27}$-NGs is even weaker than that of rGO. This confirms the GO reduction for Ni$_{40}$Au$_{33}$Pt$_{27}$-NGs is more complete than for rGO.

Electrocatalysis of NiAuPt-NGs. Ni$_{40}$Au$_{33}$Pt$_{27}$-NGs were investigated as the electrocatalysts for EOR in alkaline media. Although there have been a few reports on Pt-based trimetallic catalysts in alkaline media,[43,47−49] thoese catalysts usually do not have Ni but Ru.
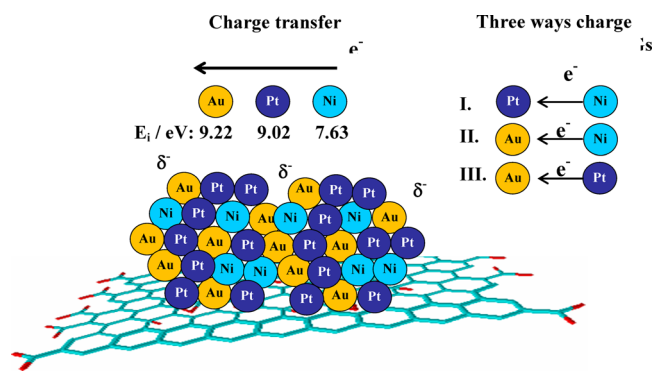
Figure 4. (a) XPS spectra of (a) Ni 3p, Au 4f, and Pt 4f. (b) Deconvolution of Ni 2p of NiAuPt-NGs. (c) Pt 4f and Au 4f XPS spectra of Pt-NGs, Au-NGs, and NiAuPt-NGs.

the Ni 2p$_{3/2}$ signal is deconvoluted into four bands at 852.7, 853.8, 855.6, and 857.3 eV, respectively. They correspond to metallic Ni and other nickel species such as NiO, Ni(OH)$_2$, and
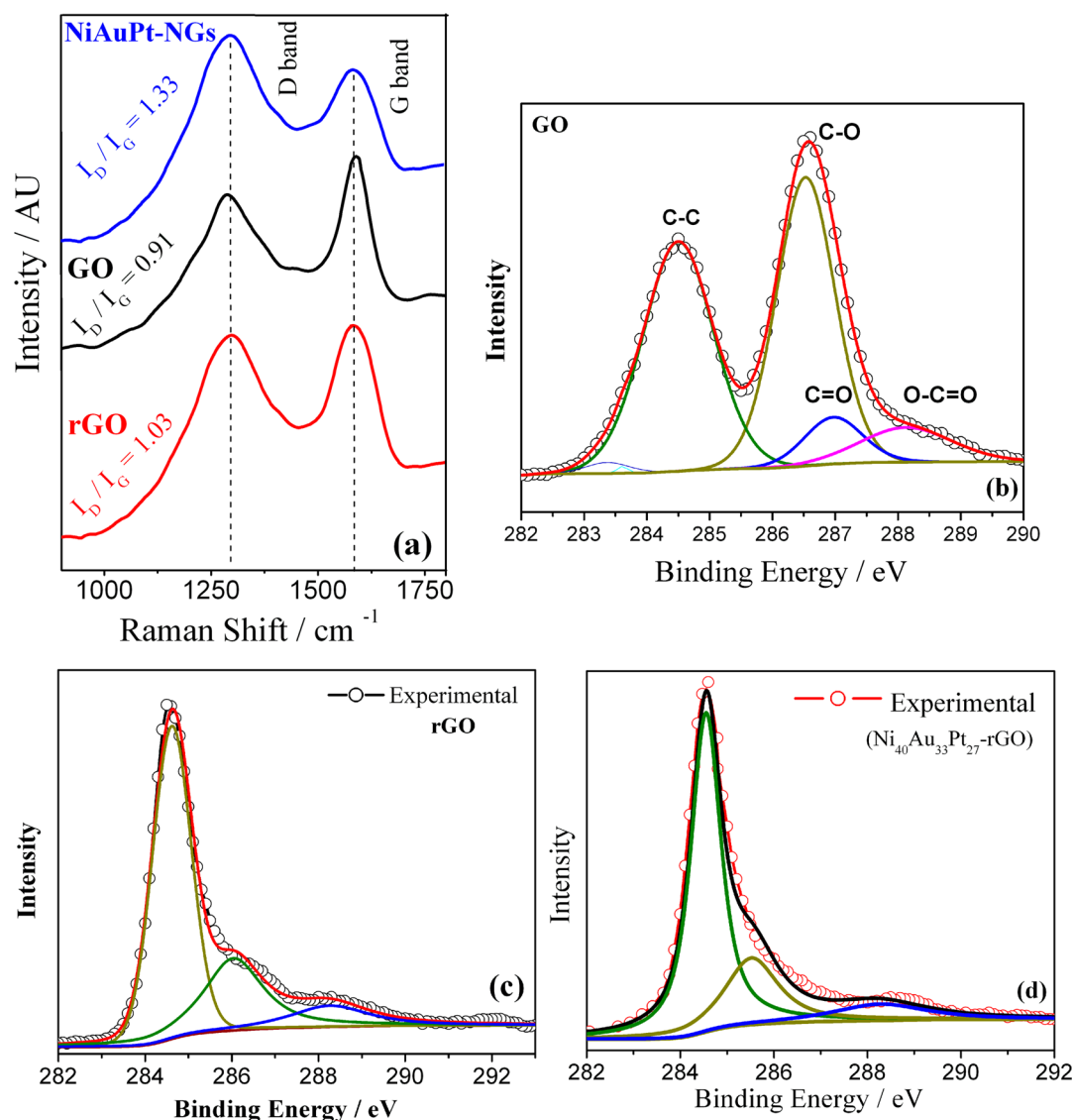
Figure 5. (a) Raman spectra of rGO, GO, and NiAuPt-NGs. C 1s XPS spectra of (b) GO, (c) rGO, and (d) NiAuPt-NGs.

Figure 6a presents the cyclic voltammograms (CVs) of the different catalysts in 0.5 M NaOH. The electrochemically active surface areas (ECSA) were calculated in terms of the oxide reduction peaks and are summarized in Table S1 in the Supporting Information. In these calculations, the required charges for the reduction of PtO, NiO, and Au_2O_3 monolayers were 420, 430, and 400 μC cm^{-2}, respectively, in terms of the literature.[6,22,43,69] The average charge required for the oxide reduction of $Ni_{40}Au_{33}Pt_{27}$ was 417.4 μC cm^{-2}, and it was used for the determination of the ECSA values. Similar calculations were made for binary metal catalysts as well. The ECSA of $Ni_{40}Au_{33}Pt_{27}$-NGs is 80.1 m^2 g^{-1}, higher than that of the binary and unary metal nanoparticles on rGO. This can be ascribed to the effect of Ni and Au in $Ni_{40}Au_{33}Pt_{27}$.

Figure 6b shows the stabilized voltammograms (60th cycle) of EOR on $Ni_{40}Au_{33}Pt_{27}$-NGs in a solution containing 1.0 M ethanol and 0.5 M KOH. The voltammograms exhibit typical EOR features in alkaline medium.[6,39] The peak current appears at 212 mV vs SHE in the forward scan and at −305 mV vs SHE in the backward scan. The current in the backward scan is primarily associated with the removal of carbonaceous species that are not completely oxidized in the forward scan. The

forward peak current density and onset oxidation potential are two important parameters to evaluate the activity of catalysts.[33] The EOR currents were normalized to the Pt mass for the bimetallic or trimetallic systems. The bimetallic $Au_{55}Pt_{45}$-NGs and $Ni_{43}Pt_{57}$-NGs, whose atomic ratios were determined by ICP-AES analysis, show higher mass specific currents than Pt-NGs and Pt/C. The trimetallic $Ni_{40}Au_{33}Pt_{27}$-NGs far exceeds the activity of all other catalysts. The peak current density of $Ni_{40}Au_{33}Pt_{27}$-NGs is significantly higher than those with other catalysts. The peak current density is 4938 mA per mg Pt for $Ni_{40}Au_{33}Pt_{27}$-NGs in the forward scan. This is much higher than that (2641 mA) of $Au_{55}Pt_{45}$-NGs, and it is about 3.6 and 8.5 times higher than those of $Ni_{43}Pt_{57}$-NGs (1361 mA) and Pt-NGs (564 mA), respectively. Moreover, in order to obtain the intrinsic catalytic activity, the oxidation currents are normalized with respect to the ECSA values of the catalysts (Figure S5 in the Supporting Information).[42] The current density with $Ni_{40}Au_{33}Pt_{27}$-NGs is 129% higher than that with Pt-NGs, 92% higher than that with $Ni_{43}Pt_{57}$-NGs, and 36% higher than that with $Au_{55}Pt_{45}$-NGs. Furthermore, the onset potential for $Ni_{40}Au_{33}Pt_{27}$-NGs is −803 mV vs SHE, much lower than those of $Au_{55}Pt_{45}$-NGs, $Ni_{43}Pt_{57}$-NGs, and Pt-NGs (Figure 6c). The
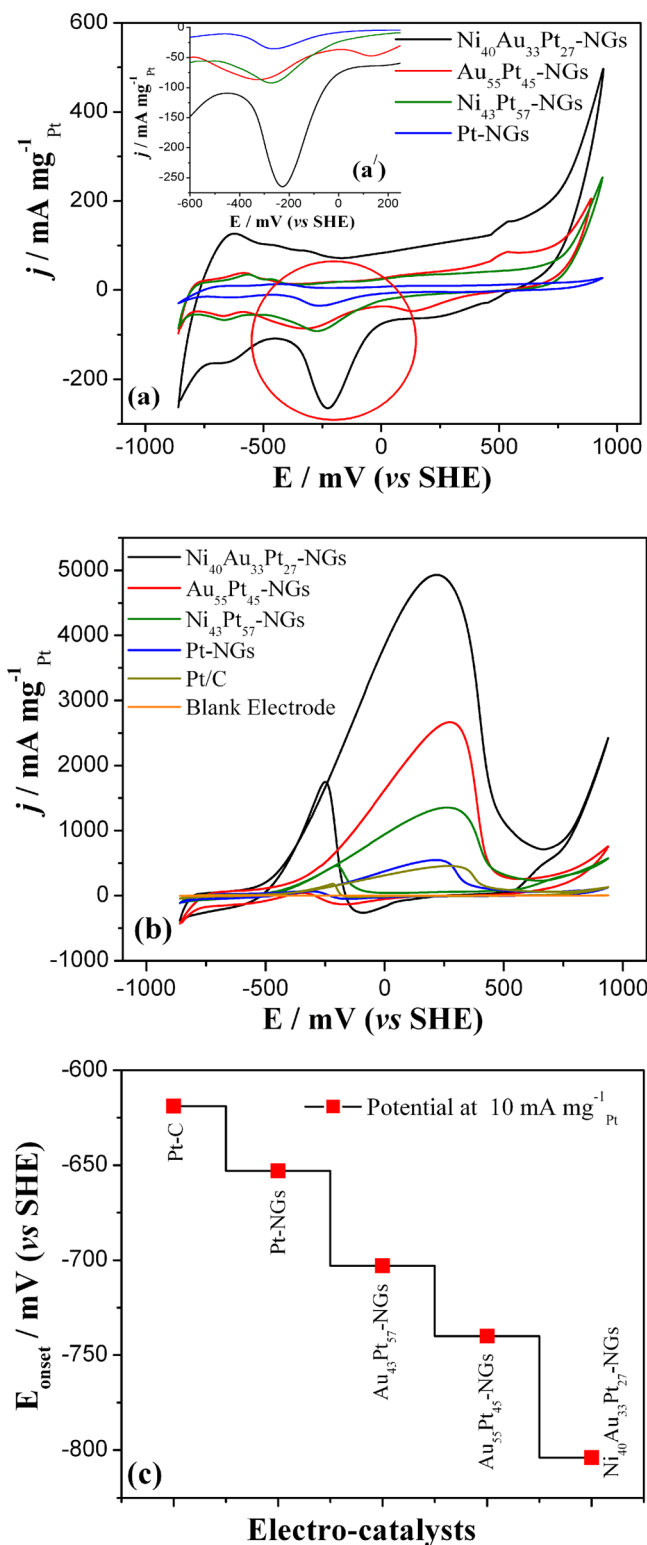
Figure 6. (a) CVs of electrocatalysts in 0.5 M NaOH. (b) Mass specific current of the 60th cycle of CVs of EOR with different catalysts in a solution containing 1.0 M ethanol and 0.5 M NaOH at room temperature. The scan rate was 10 mV s^{-1}. (c) Respective oxidation potential of the different catalysts at 10 mA/mg of Pt.
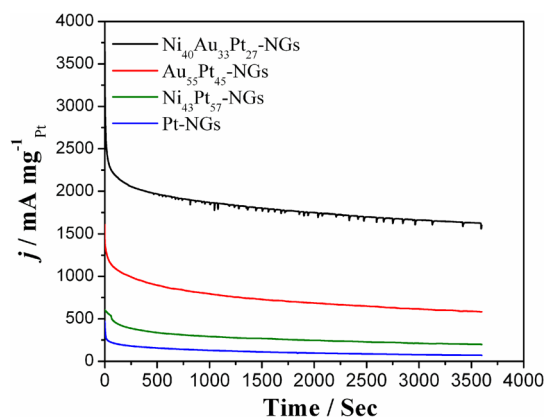

Figure 7. Chronoamperograms with different catalysts in a solution containing 0.5 M NaOH and 1 M ethanol at −160 mV vs SHE. The currents are normalized to the Pt loadings.
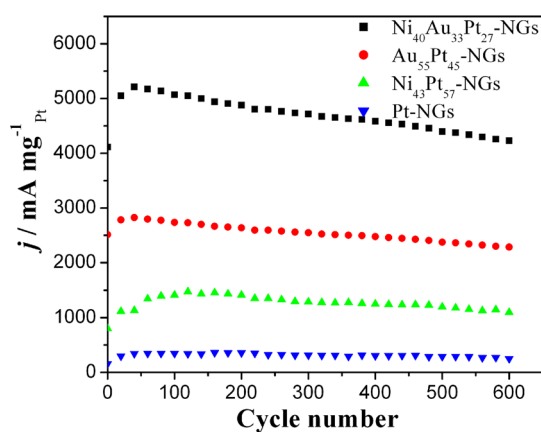

Figure 8. Variation of the peak current density of EOR in the forward scan with the CV cycle number for Ni$_{40}$Au$_{33}$Pt$_{27}$-NGs, Au$_{55}$Pt$_{45}$-NGs, Ni$_{43}$Pt$_{57}$-NGs, and Pt-NGs in a solution containing 1.0 M EtOH and 0.5 M NaOH solution. The currents are normalized to the Pt loadings.

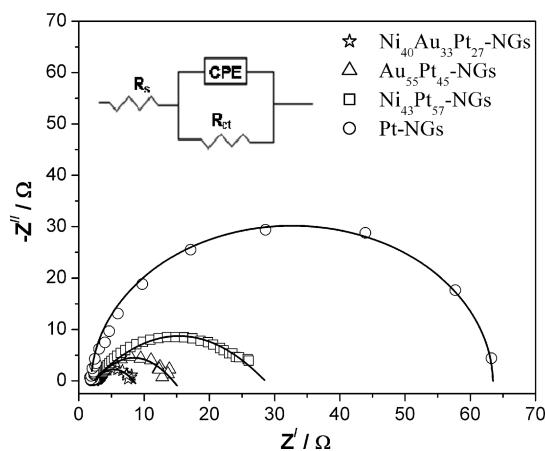**Figure 9.** Electrochemical impedance spectroscopy of ethanol electro-oxidation in a solution containing 1.0 M ethanol and 0.5 M NaOH with Ni$_{40}$Au$_{33}$Pt$_{27}$-NGs, Au$_{55}$Pt$_{45}$-NGs, Ni$_{43}$Pt$_{57}$-NGs, and Pt-NGs at a potential of −160 mV vs SHE. The inset gives the equivalent circuit.

low onset potential signifies the easy oxidation of ethanol on the surface of Ni$_{40}$Au$_{33}$Pt$_{27}$-NGs.

The high catalytic activity of Ni$_{40}$Au$_{33}$Pt$_{27}$-NGs can be attributed to the synergetic effects of the three types of metal

elements. CH$_3$CO$_{ads}$ or other reactive intermediates can strongly adsorb on the surface of Pt and thus block the catalytic sites.[31,65] The effect of the Au element can be considered as the results of the catalysis of nanostructured Au

toward the oxidation of CO.[41−43] Ni can also prevent the CO adsorbance on Pt, because the OH groups of $Ni(OH)_2$ can prevent the adsorbance of CO and other intermediates. In addition, nickel oxides and nickel hydroxides can generate additional OH^- groups through the autocatalytic reaction[70]

$$Ni(OH)_2 \rightarrow NiO + H_2O$$

or

$$Ni(OH)_2 \rightarrow NiOOH + H^+ + e^- \leftrightarrow NiO + OH^- + H^+$$
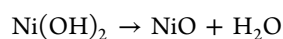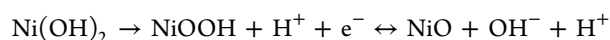
Apart from the effect of the individual metal, the charge transfer among the tightly coupled metallites can also improve the catalytic activity.[73,74] The negatively charged Au of $Ni_{40}Au_{33}Pt_{27}$-NGs can promote the adsorption of oxygen, which helps the complete oxidation of ethanol and prohibits the buildup of CO_{ads} on the catalyst surface.[75,76]

Chronoamperometric experiments were carried out to understand the long-term stability and the antipoisoning capability of $Ni_{40}Au_{33}Pt_{27}$-NGs, $Ni_{43}Pt_{57}$-NGs, $Au_{55}Pt_{45}$-NGs, and Pt-NGs. The experiments were performed in a solution containing 0.5 M NaOH and 1.0 M ethanol at a potential of −160 mV over a period of 3600 s (Figure 7). The current decays at the beginning for all of the catalysts. This is attributed to the accumulation of intermediate species during EOR.[6,43,65] However, $Ni_{40}Au_{33}Pt_{27}$-NGs always gives rise to current density much higher than that of other catalysts. This confirms that $Ni_{40}Au_{33}Pt_{27}$-NGs is more stable and has poisoning-tolerance ability superior to that of the other catalysts.

The catalytic activities in terms of the polarization current densities are in the order $Ni_{40}Au_{33}Pt_{27}$-NGs > $Au_{55}Pt_{45}$-NGs > $Ni_{43}Pt_{57}$-NGs > Pt-NGs. This indicates that the incorporation of Ni and Au into Pt decreases the poisoning effect and facilitates the cleavage of the C−C bond of the adsorbed intermediates during EOR.[6,44,69] This is consistent with the CV results. The previous studies on the catalysis of PtAu and PdNi also suggest that Au and Ni could facilitate the cleavage of the C−C bond.[44,69]

An accelerated stability was tested for the catalysts toward EOR. CVs were performed for 600 cycles at a scan rate of 50 mV s^{-1} using $Ni_{40}Au_{33}Pt_{27}$-NGs, $Au_{55}Pt_{45}$-NGs, $Ni_{43}Pt_{57}$-NGs, and Pt-NGs as the catalysts in a solution containing 1.0 M ethanol and 0.5 M KOH. Figure 8 shows the variation of the EOR peak current density in the forward scan with the CV number. Initially, the peak current density increases and then gradually decreases with the increase of the scan number. The peak current densities per mg Pt at the 600th scan are 4236, 2316, 1102, and 286 mA for $Ni_{40}Au_{33}Pt_{27}$-NGs, $Au_{55}Pt_{45}$-NGs, $Ni_{43}Pt_{57}$-NGs, and Pt-NGs, respectively. These current densities are lower than their corresponding maximum current densities by 8.9%, 13.6%, 16.9% and 45.6%, respectively. These further confirm that NiAuPt-NGs have better electrocatalytic performance and higher stability toward EOR than the other catalysts.

Electrochemical impedance spectroscopy (EIS) was used to investigate the interfacial processes and kinetics of electrode reactions. Figure 9 presents the Nyquist plots for EOR at −160 mV with various catalysts in a solution containing 0.5 M NaOH and 1.0 M ethanol. The Bode plots are presented in Figure S6 in the Supporting Information. The impedance data was analyzed by using the NOVA Version 1.10 software with the equivalent circuits shown in the inset of Figure 9. R_s is the series resistance, R_{ct} is the charge transfer resistance associated with EOR, and CPE is the double-layer capacitance. The diameter of

the arc decreases in the order Pt-NGs > $Au_{55}Pt_{45}$-NGs > $Ni_{43}Pt_{57}$-NGs > $Ni_{40}Au_{33}Pt_{27}$-NGs. The R_{ct} value with $Ni_{40}Au_{33}Pt_{27}$-NGs is 6.93 Ω, much lower than that of Pt-NGs (61.11 Ω) and other binary species ($Ni_{43}Pt_{57}$-NGs, 26.37 Ω; $Au_{55}Pt_{45}$-NGs, 14.39 Ω). This also indicates the high catalytic activity of the former in comparison to that of the latter. The lower charger transfer resistance of $Ni_{40}Au_{33}Pt_{27}$-NGs can be attributed to the prevention of the intermediate adsorption on the catalyst surface. The OH^- groups on the catalyst surface promote the oxidation kinetics and thus lower the charge transfer resistance. The R_{ct} values of the binary catalysts are also remarkably lower than that of Pt-NGs.

4. CONCLUSIONS

$Ni_{40}Au_{33}Pt_{27}$-NGs is synthesized through the simultaneous reduction of GO and three metal precursors. The trimetallic nanoparticles have a narrow size distribution. There are tightly coupled structures with Ni-rich, Au-rich, and Pt-rich phases. They exhibit higher electrocatalytic activity toward EOR in alkaline media than the binary or unary metallic catalysts. The electrochemical techniques reveal that $Ni_{40}Au_{33}Pt_{27}$-NGs drastically increases the peak current density for EOR and significantly shifts the onset potential to negative. The trimetallic catalysts also exhibit better CO tolerance than the binary and unary catalysts. The charge-transfer resistance for EOR on the $Ni_{40}Au_{33}Pt_{27}$-NGs is much less than that for the other catalysts as well.

■ ASSOCIATED CONTENT

Ⓢ Supporting Information

The following file is available free of charge on the ACS Publications website at DOI: 10.1021/cs501365y.

TGA, XRD, ICP-AES, and TEM analysis and electrochemistry data of the synthesized nanoparticles (PDF)

■ AUTHOR INFORMATION

Corresponding Author

*J.O.: fax, +65-6776 3604; tel, +65-6516 1472; e-mail, mseoj@nus.edu.sg.

Present Address

†(For A.D.) Electrochemical & Nanoscience research group, Department of Chemistry & Biochemistry, University of Bern, Bern, Switzerland. E-mail: ad.chem@yahoo.com.

Notes

The authors declare no competing financial interest.

■ REFERENCES

(1) Hsieh, Y. C.; Zhang, Y.; Su, D.; Volkov, V.; Si1, R.; Wu, L.; Zhu, Y.; An, W.; Liu, P.; He, P.; Ye, S.; Adzic, R. R.; Wang, J. X. *Nat. Commun.* **2013**, *4*, 2466.

(2) Li, M.; Cullen, D. A.; Sasaki, K.; Marinkovic, N. S.; More, K.; Adzic, R. R. *J. Am. Chem. Soc.* **2013**, *135*, 132−141.

(3) Zhao, J.; Shao, M.; Yan, D.; Zhang, S.; Lu, Z.; Li, Z.; Cao, X.; Wang, B.; Wei, M.; Evansa, D. G.; Duan, X. *J. Mater. Chem. A* **2013**, *1*, 5840−5846.

(4) Antolini, E. *J. Power Sources* **2007**, *170*, 1−12.

(5) Song, S. Q.; Tsiakaras, P. *Appl. Catal., B* **2006**, *63*, 187−193.

(6) Datta, J.; Dutta, A.; Mukherjee, S. *J. Phys. Chem. C* **2011**, *115*, 15324−15334.

(7) Wasmus, S.; Kuver, A. *J. Electroanal. Chem.* **1999**, *461*, 14−31.

(8) Bockris, J.; Reddy, A. K. N.; Aldeco, M. *Modern Electrochemistry*, 2nd ed.; ; Kluwer Academic: New York, 2002; Vol. 2A.

(9) Lai, S. C. S.; Koper, M. T. M. *Phys. Chem. Chem. Phys.* **2009**, *11*, 10446−10456.

(10) Shimazu, K.; Uosaki, K.; Kita, H.; Nodasaka, Y. *J. Electroanal. Chem.* **1988**, *256*, 481−487.

(11) Arico, A. S.; Srinivasan, S.; Antonucci, V. *Fuel Cells* **2001**, *1*, 133−161.

(12) Markovic, N.; Gasteiger, H. A.; Ross, P. N.; Jiang, X. D.; Villegas, I.; Weaver, M. J. *Electrochim. Acta* **1995**, *40*, 91−98.

(13) Mazumder, V.; Lee, Y.; Sun, S. H. *Adv. Funct. Mater.* **2010**, *20*, 1224−1231.

(14) Kowal, A.; Li, M.; Shao, M.; Sasaki, K.; Vukmirovic, M. B.; Zhang, J. N.; Marinkovic, S.; Liu, P.; Frenkel, A. I.; Adzic, R. R. *Nat. Mater.* **2009**, *8*, 325−330.

(15) Tsiakaras, P. E. *J. Power Sources* **2007**, *171*, 107−112.

(16) Yin, S.; Yang, L.; Luo, L.; Huang, F.; Qiang, Y.; Zhang, H.; Yan, Z. *New J. Chem.* **2013**, *37*, 3976−3980.

(17) Ammam, M.; Easton, E. B. *J. Electrochem. Soc.* **2012**, *159*, B635−B640.

(18) Yang, B.; Lu, Q.; Wang, Y.; Zhuang, L.; Lu, J.; Liu, P.; Wang, J.; Wang, R. *Chem. Mater.* **2003**, *15*, 3552−3557.

(19) Riveros, L. L. T.; Blas, R. G.; Torres, A. E. M.; Prelas, M.; Tryk, D. A.; Cabrera, C. R. *ACS Appl. Mater. Interfaces* **2012**, *4*, 1134−1147.

(20) Wang, Z. B.; Zuo, P. J.; Wang, G. J.; Du, C. Y.; Yin, G. P. *J. Phys. Chem. C* **2008**, *112*, 6582−6587.

(21) Chung, Y.; Pak, C.; Park, G. S.; Jeon, W. S.; Kim, J. R.; Lee, Y.; Chang, H.; Seung, D. *J. Phys. Chem. C* **2008**, *112*, 313−318.

(22) Dutta, A.; Datta, J. *Int. J. Hydrogen Energy* **2013**, *38*, 7789−7800.

(23) Jeon, M. K.; Won, J. Y.; Oh, K. S.; Lee, K. R.; Woo, S. I. *Electrochim. Acta* **2007**, *53*, 447−452.

(24) Jeon, M. K.; Lee, K. R.; Oh, K. S.; Hong, D. S.; Won, J. Y.; Li, S.; Woo, S. I. *J. Power Sources* **2006**, *158*, 134−137.

(25) Antolini, E. *Energy Environ. Sci.* **2009**, *2*, 915−931.

(26) Chueh, W. C.; Hao, Y.; Jung, W. C.; Haile, S. M. *Nat. Mater.* **2012**, *11*, 155−161.

(27) Shen, P. K.; Xu, C. *Electrochem. Commun.* **2006**, *8*, 184−188.

(28) Wang, T.; Mpourmpakis, G.; Lonergan, W. W.; Vlachosb, D. G.; Chen, J. G. *Phys. Chem. Chem. Phys.* **2013**, *15*, 12156−12164.

(29) Wang, Z. B.; Yin, G. P.; Zhang, J.; Sun, Y. C.; Shi, P. F. *J. Power Sources* **2006**, *160*, 37−44.

(30) Chelaghmia, M. L.; Nacef, M.; Affoune, A. M. *J. Appl. Electrochem.* **2012**, *42*, 819−826.

(31) Mu, R.; Fu, Q.; Xu, H.; Zhang, H.; Huang, Y.; Jiang, Z.; Zhang, S.; Tan, D.; Bao, X. *J. Am. Chem. Soc.* **2011**, *133*, 1978−1986.

(32) Paulus, U. A.; Wokaun, A.; Scherer, G. G.; Schmidt, T. J.; Stamenkovic, V.; Radmilovic, V.; Markovic, N. M.; Ross, P. N. *J. Phys. Chem. B* **2002**, *106*, 4181−4191.

(33) Park, K. W.; Choi, J. H.; Kwon, B. K.; Lee, S. A.; Sung, Y. E.; Ha, H. Y.; Hong, S. A.; Kim, H. S.; Wieckowski, A. *J. Phys. Chem. B* **2002**, *106*, 1869−1877.

(34) Loukrakpam, R.; Luo, J.; He, T.; Chen, Y.; Xu, Z.; Njoki, P. N.; Wanjala, B. N.; Fang, B.; Mott, D.; Yin, J.; Klar, J.; Powell, B.; Zhong, C. J. *J. Phys. Chem. C* **2011**, *115*, 1682−1694.

(35) Deivaraj, T. C.; Chen, W. X.; Lee, J. Y. *J. Mater. Chem.* **2003**, *13*, 2555−2560.

(36) Park, K. W.; Choi, J. H.; Sung, Y. E. *J. Phys. Chem. B* **2003**, *107*, 5851−5856.

(37) Yang, G.; Li, Y.; Ranab, R. K.; Zhu, J. J. *J. Mater. Chem. A* **2013**, *1*, 1754−1762.

(38) Liang, Z. X.; Zhao, T. S. Catalysts for Alcohol-Fuelled Direct Oxidation Fuel Cells. In *RSC Energy and Environment Series*; Royal Society of Chemistry: London, 2012; Vol. 6.

(39) Zhang, J.; Sasaki, K.; Sutter, E.; Adzic, R. R. *Science* **2007**, *315*, 220−222.

(40) Ren, F.; Wang, C.; Zhai, C.; Jiang, F.; Yue, R.; Du, Y.; Yang, P.; Xu, J. *J. Mater. Chem. A* **2013**, *1*, 7255−7261.

(41) Liang, Z. X.; Zhao, T. S.; Xu, J. B. *J. Power Sources* **2008**, *185*, 166−170.

(42) Yang, L.; Yang, W.; Cai, Q. *J. Phys. Chem. C* **2007**, *111*, 16613−16617.

(43) Dutta, A.; Mahapatra, S. S.; Datta, J. *Int. J. Hydrogen Energy* **2011**, *36*, 14898−14906.

(44) Dutta, A.; Ouyang, J. *Appl. Catal., B* **2014**, *158−159*, 119−128.

(45) Zheng, H.; Neo, C. Y.; Mei, X.; Qiu, J.; Ouyang, J. *J. Mater. Chem.* **2012**, *22*, 14465−14474.

(46) Mei, X.; Zheng, H.; Ouyang, J. *J. Mater. Chem.* **2012**, *22*, 9109−9116.

(47) Stamenkovic, V. B.; Moon, S. K.; Mayerhofer, J.; Ross, P. N.; Markovic, N.; Rossmeisl, J.; Greeley, J.; Norskov, J. K. *Angew. Chem., Int. Ed.* **2006**, *45*, 2897−2901.

(48) Bambagioni, V.; Bianchini, C.; Filippi, J.; OberhauserIal, W.; Marchionni, A.; Vizza, F.; Psaro, R.; Sordelli, L.; Foresti, M. L.; Innocenti, M. *ChemSusChem* **2009**, *2*, 99−112.

(49) Shen, S.; Zhao, T. S.; Xu, J.; Li, Y. *Energy Environ. Sci.* **2011**, *4*, 1428−1433.

(50) Chen, X.; Su, B.; Wu, G.; Yang, C. J.; Zhuang, Z.; Wang, X.; Chen, X. *J. Mater. Chem.* **2012**, *22*, 11284−11289.

(51) Geim, A. K.; Novoselov, K. S. *Nat. Mater.* **2007**, *6*, 183−191.

(52) Su, Y.; Lu, X.; Xie, M.; Geng, H.; Wei, H.; Yang, Z.; Zhang, Y. *Nanoscale* **2013**, *5*, 8889−8893.

(53) Bonaccorso, F.; Sun, Z.; Hasan, T.; Ferrar, A. C. *Nat. Photonics* **2010**, *4*, 611−622.

(54) Kim, K. S.; Zhao, Y.; Jang, H.; Lee, S. Y.; Kim, J. M.; Ahn, J. H.; Kim, P.; Choi, J. Y.; Hong, B. H. *Nature* **2009**, *457*, 706−710.

(55) Berger, C.; Song, Z. M.; Li, X. B.; Wu, X. S.; Brown, N.; Naud, C.; Mayou, D.; Li, T. B.; Hass, J.; Marchenkov, A. N.; Conrad, E. H.; First, P. N.; de Heer, W. A. *Science* **2006**, *312*, 1191−1196.

(56) Guo, S. J.; Dong, S. J.; Wang, E. K. *ACS Nano* **2010**, *4*, 547−555.

(57) Fan, X. B.; Peng, W. C.; Li, Y.; Li, X. Y.; Wang, S. L.; Zhang, G. L.; Zhang, F. B. *Adv. Mater.* **2008**, *20*, 4490−4493.

(58) Rao, C. V.; Cabrera, C. R.; Ishikawa, Y. *J. Phys. Chem. C* **2011**, *115*, 21963−21970.

(59) Hummers, W.; Re, O. *J. Am. Chem. Soc.* **1958**, *80*, 1339−1339.

(60) Mei, X.; Ouyang, J. *Carbon* **2011**, *49*, 5389−5397.

(61) Guerin, S.; Hayden, B. E.; Lee, C. E.; Mormiche, C.; Russell, A. E. *J. Phys. Chem. B* **2006**, *110*, 14355−14362.

(62) Xu, C.; Tian, Z.; Chen, Z.; Jiang, S. P. *Electrochem. Commun.* **2008**, *10*, 246−249.

(63) He, Q.; Chen, W.; Mukerjee, S.; Chen, S.; Laufek, F. *J. Power Sources* **2009**, *187*, 298−304.

(64) Chen, S. D.; Zhao, J. *Int. J. Electrochem. Sci.* **2013**, *8*, 678−688.

(65) Basu, D.; Basu, S. *Int. J. Hydrogen Energy* **2012**, *37*, 4678−4684.

(66) Wang, Z. B.; Zuo, P. J.; Wang, G. J.; Du, C. Y.; Yin, G. P. *J. Phys. Chem. C* **2008**, *112*, 6582−6587.

(67) Park, K. W.; Choi, J. H.; Kwon, B. K.; Lee, S. A.; Sung, Y. E.; Ha, H. Y.; Hong, S. A.; Kim, H. H.; Wieckowski, A. *J. Phys. Chem. B* **2002**, *106*, 1869−1877.

(68) Wang, Y. X.; Zhang, S.; Lee, J. W.; Lewd, W. S.; Li, B. *Appl. Surf. Sci.* **2013**, *265*, 418−423.

(69) Dutta, A.; Datta, J. *J. Mater. Chem. A* **2014**, *2*, 3237−3250.

(70) Shen, S. Y.; Zhao, T. S.; Xu, J. B.; Li, Y. S. *J. Power Sources* **2010**, *195*, 1001−1006.

(71) Yao, Z. Q.; Zhu, M. S.; Jiang, F. X.; Du, Y. K.; Wang, C. Y.; Yang, P. *J. Mater. Chem.* **2012**, *22*, 13707−13713.

(72) Guo, H. L.; Wang, X. F.; Qian, Q. Y.; Wang, F. B.; Xia, X. H. *ACS Nano* **2009**, *3*, 2653−2659.

(73) Naumenko, D.; Snitka, V.; Snopok, B.; Arpiainen, S.; Lipsanen, H. *Nanotechnology* **2012**, *23*, 465703.

(74) Guo, X.; Brault, P.; Zhi, G.; Caillard, A.; Jin, G.; Coutanceau, C.; Baranton, S.; Guo, X. *J. Phys. Chem. C* **2011**, *115*, 11240−11246.

(75) Liu, M.; McAllister, B.; Ye, H. Q.; Hu, P. *J. Am. Chem. Soc.* **2006**, *128*, 4017−4022.

(76) Dutta, A.; Datta, J. *J. Phys. Chem. C* **2012**, *116*, 25677−25688.